# Performance Characterization of Tightly-Coupled GNSS Precise Point Positioning Inertial Navigation within a Simulation Environment

Ryan M. Watson,* Victor Sivaneri,* and Jason N. Gross†

*West Virginia University, Morgantown,WV, 26506, USA*

UAVs have the potential for autonomous airborne remote sensing applications that require rapid response to natural hazards (e.g.. volcano eruptions, earthquakes). As these applications require very accurate positioning, such as airborne Synthetic Aperture Radar, tightly coupled Global Positioning System (GPS) Precise Point Positioning (PPP) Inertial Navigation Systems (INS) are an attractive method to perform real-time aircraft positioning. In particular, PPP can achieve a level of positioning accuracy that is similar to Real-Time Kinematic (RTK) GPS, without the need of a relatively close GPS reference station. However, the PPP method is known to converge to accurate positioning more slowly when compared to RTK, a drawback of PPP that is amplified whenever the receiver platform is faced with GPS challenged environments, such as poor satellite visibility and frequent phase breaks. Unfortunately, these challenging conditions occur more often when the platform being positioned is an aircraft that experiences abrupt changes in attitude. In this paper we present the use of a simulation environment to characterize the position estimation performance sensitivity of PPP/INS through a Monte Carlo analysis that is considered under various conditions, such as: the intensity of multipath errors, the number of phase breaks that occur in a flight, satellite geometry, atmospheric conditions, noise characteristics and grade of the inertial sensor, and accuracy of GPS orbit products.

## Nomenclature

$\mathbf{x}$ = State Vector
$\psi$ = Attitude ($radians$)
$v$ = Velocity ($meters/second$)
$r$ = Position ($meters$)
$R$ = Geometric Range ($meters$)
$C$ = Coordinate Transformation Matrix
$\rho$ = Pseudorange ($meters$)
$\phi$ = Carrier-Phase ($meters$)
$c$ = Speed of light ($meters/second$)
$\delta\theta$ = Delta Angle ($radians$)
$\delta v$ = Delta Velocity ($meters/second$)
$el$ = User to Satellite Elevation Angle ($radians$)
$F$ = System Matrix
$\Phi$ = State Transition Matrix
$\tau$ = Time Step ($second$)
$\phi$ = Roll ($radians$)
$\theta$ = Pitch ($radians$)
$\psi$ = Yaw ($radians$)
$\omega_e$ = Earth Rotation Rate ($radians/second$)
$Lat$ = Latitude ($radians$)

---

*Graduate Research Assistant,Department of Mechanical and Aerospace Engineering, P.O. 6106, AIAA Student Member
†Assistant Professor, Department of Mechanical and Aerospace Engineering, P.O. 6106, AIAA Senior Member

American Institute of Aeronautics and Astronautics

$Lon$ = Longitude (*radians*)
$H$   = Height (*meters*)

# I.  Introduction

THE Precise Point Positioning (PPP) approach uses dual-frequency undifferenced GPS observables in conjunction with precise orbit and clock bias products and measurement models to achieve decimeter to centimeter level positioning with a single receiver.[1] Real-time PPP is enabled by orbit and clock products being broadcast to end user. These global correctors have been integrated into the L-band by commercial entities,[2] can be obtained over the internet or through an Iridium modem link from NASA's Global Differential GPS System,[3] and have recently been made freely available on the internet by the International GNSS Service.[4] The similar level of accuracy of real-time PPP compared to traditional Differential GPS (DGPS) (i.e. Real Time Kinematic) without the need for a nearby static GPS reference station, is particularly attractive for airborne scientific instrument platforms that require this level of accuracy, global coverage and rapid response capability. For instance, real-time PPP is used for NASA's airborne Synthetic Aperture Radar (SAR) platforms that are used for repeat pass interferometry in response to natural hazzards such as volcano eruptions, tsunamis, and large earthquakes.[5]

The benefits of coupling GPS with Inertial Navigation Systems (INS) have long been well understood,[6] and recent studies have investigated and demonstrated combined PPP/INS architectures for kinematic applications on ground vehicles,[7],[8],[9],[10] and airborne platforms.[10] In these previous works, both loosely-coupled and tightly-coupled architectures have been investigated, and when provided clear open sky-access and on vehicles with docile dynamics, both approaches have shown to exhibit similar estimation performance,[9].[10] However, when confronted with challenging GPS environments, such as poor visibility (e.g. urban canyon), frequent phase breaks, and high-multipath, tightly-coupled formulations inherently have the advantage,[9].[10]

Rapidly deployable Unmanned Aerial Vehicle (UAV) platforms are attractive for many applications that require precise positioning, and the flexibility for deployment anywhere on the Earth, but often suffer from aforementioned environmental conditions that are unfavorable for achieving optimal PPP performance. In particular, UAVs typically have fast dynamics (i.e. roll angles approaching $45°$ are not uncommon), which induces poor satellite geometry, increases the likelihood of phase breaks, and lends itself to the need of tightly-coupled PPP/INS for precise kinematic positioning of a UAVs. In this paper, we characterize the expected performance of PPP/INS when faced with several conditions that are well known to be challenging for PPP, and we also assess the impact of various grade inertial sensors.

The rest of this paper is organized as follows, Section II. details the PPP/INS formulation used and Section III. describes the simulation environment used for this study as well as the design of the Monte Carlo study. Section IV. summarizes the results and Section V. offers the conclusions of this work and discusses future plans for implementation and experimental evaluation in NASA JPL's GIPSY-OASIS software,[11].[12]

# II.  Algorithm Formulation

This section gives a brief overview of the formulations used in this paper. First an overview of the PPP observation model. Then the mechanization of the Inertial Measurement Unit (IMU) data in the inertial frame is covered. Finally, the Extended Kalman Filter used to combine the GPS and IMU data is discussed.

## A.  PPP Observation Model

The PPP approach utilizes dual-frequency undifferenced GPS observables. Because undifferenced data is being used, methods for mitigating GPS error sources (e.g., ionospheric delay, tropospheric delay, and receiver clock delay), which are canceled through data differing with traditional Differential GPS (DGPS), must be incorporated in the measurement models.

To mitigate the ionospheric delay, the dispersive nature of the ionosphere is leveraged, and a linear combination of the GPS $L_1$ and $L_2$ frequencies (1575.42 MHz and 1227.60 MHz, respectively) is formed to produce ionospheric-free (IF) pseudorange and carrier phase measurements.[13] The IF combination for psuedorange and carrier-phase can be seen in Eq. 1 and Eq. 2, respectively.

American Institute of Aeronautics and Astronautics

$$\rho^j_{IF} = \rho^j_{L1}\left[\frac{f_1^2}{f_1^2 - f_2^2}\right] - \rho^j_{L2}\left[\frac{f_1^2}{f_1^2 - f_2^2}\right] = 2.546\rho^j_{L1} - 1.546\rho^j_{L2} \tag{1}$$

$$\phi^j_{IF} = \phi^j_{L1}\left[\frac{f_1^2}{f_1^2 - f_2^2}\right] - \phi^j_{L2}\left[\frac{f_1^2}{f_1^2 - f_2^2}\right] = 2.546\phi^j_{L1} - 1.546\phi^j_{L2} \tag{2}$$

In Eq. 1 and Eq. 2 the $f_1$ and $f_2$ are the $L_1$ and $L_2$ frequencies, $\rho_{L1}$ and $\rho_{L2}$ are the pseudorange measurements on the $L_1$ and $L_2$ frequencies, $\phi_{L1}$ and $\phi_{L2}$ are the carrier-phase measurements on the $L_1$ and $L_2$ frequencies. The superscript $j$ in Eq. 1 and Eq. 2 is used to designate the measurement between the platform and satellite $j$.

Using the IF combination, the pseudorange and carrier-phase measurements are modeled as shown in Eq. 3 and Eq. 4, respectively: where $\delta t_u$ is the receiver's clock bias, $T_z$ is the tropospheric delay in the zenith direction, $m(el^j)$ is a user to satellite elevation angle dependent mapping function, $\lambda_{IF}$ is the wavelength corresponding to the IF combination, and $N_{IF}$ is phase ambiguity. The geometric range between the platform and the satellite is denoted as $R^j$, and given as $R^j = \sqrt{(x^j - x_u)^2 + (y^j - y_u)^2 + (z^j - z_u)^2}$, where the subscript $u$ represents the platforms position, and the superscript $j$ represents the satellite, both in the same cartesian reference frame.

$$\rho^j_{IF} = R^j + c\delta t_u + T_z m(el.^j) + \epsilon^j_\rho \tag{3}$$

$$\phi^j_{IF} = R^j + c\delta t_u + T_z m(el^j) + \lambda_{IF} N^j_{IF} + \epsilon^j_\phi \tag{4}$$

In Eqs. 3 and 4 the remaining unmodelled error sources are indicated with $\epsilon$. In addition, the tropospheric delay $T_z$ in Eqs. 3 and 4 is composed of both a wet and dry components. In practice, the dry delay makes up the majority of the total zenith path tropospheric delay (i.e. $\approx 2.5$ meters) and can be well modeled. The wet delay is on the order to 10% the dry delay and is typically estimated. Within this study, the Hoppfield model[14] is used to model the dry component of the troposphere and an estimated parameters is used to compensate for the residual error of the dry delay model and wet delay. The mapping function used for this study was selected from Misra and Enge[13] and is given in Eq. 5.

$$m(el^j) = \frac{1.001}{\sqrt{0.002001 + sin(el^j)^2}} \tag{5}$$

In general, it should be noted that PPP observational models for moving platforms typically include corrections for relativistic effects (i.e. from the GPS broadcast correction), receiver and satellite antenna phase center variation, and carrier-phase wind-up, however, these effects were neglected within this simulation study.

## B. Inertial Navigation System Mechanization

Sometimes the terms are used interchangeably, in this paper, an IMU is used to denote a set of of three orthogonal accelerometers and three orthogonal gyroscopes and INS is the processing of IMU data on a navigation computer. The mechanization of INS can be broken up into four steps: attitude update, specific force transformation, velocity update, and position update. The specific details of the mechanization selected for this study are described next.

### 1. Attitude Update

To perform the attitude update, a third order Runge-Kutta method for quaternion integration, provided by Jekeli,[15] is used in order to limit the algorithmic integration errors to the fourth order. The quaternion is updated using Eq. 6: where $I$ is a 4x4 identity matrix, $\beta$ is a matrix composed of the delta angles measured with the gyroscopes and can be seen in Eq. 7, the subscript $t$ signifies the discrete samples (e.g. $t-2$ is using data from two time steps previous) .

$$\hat{q}_t = [I + \frac{1}{12}(\hat{B}_t + 4\hat{B}_{t-1} + \hat{B}_{t-2}) + \frac{1}{12}(I + \frac{1}{4}\hat{\beta}_t)\hat{\beta}_{t-1}\hat{\beta}_{t-2} + \frac{1}{12}\hat{\beta}_t(\hat{\beta}_{t-1} - \frac{1}{2}\hat{\beta}_{t-2})]\hat{q}_{t-2} \tag{6}$$

In Eq. 7 $n$ takes an integer value of 1, 2, or 3.

$$\hat{\beta}_{t+1-n} = \begin{bmatrix} 0 & (3(\delta\theta_1)_{t+1-n}-(\delta\theta_1)_{t-n}) & (3(\delta\theta_2)_{t+1-n}-(\delta\theta_2)_{t-n}) & (3(\delta\theta_3)_{t+1-n}-(\delta\theta_3)_{t-n}) \\ (-3(\delta\theta_1)_{t+1-n}+(\delta\theta_1)_{t-n}) & 0 & (3(\delta\theta_3)_{t+1-n}-(\delta\theta_3)_{t-n}) & (-3(\delta\theta_2)_{t+1-n}+(\delta\theta_2)_{t-n}) \\ (-3(\delta\theta_2)_{t+1-n}+(\delta\theta_2)_{t-n}) & (-3(\delta\theta_3)_{t+1-n}+(\delta\theta_3)_{t-n}) & 0 & (3(\delta\theta_1)_{t+1-n}-(\delta\theta_1)_{t-n}) \\ (-3(\delta\theta_3)_{t+1-n}+(\delta\theta_3)_{t-n}) & (3(\delta\theta_2)_{t+1-n}-(\delta\theta_2)_{t-n}) & (-3(\delta\theta_1)_{t+1-n}+(\delta\theta_1)_{t-n}) & 0 \end{bmatrix} \tag{7}$$

The platform's body to inertial direction cosine matrix (DCM) is related to the updated quaternion of the form $\hat{q}_t = [a,b,c,d]^T$ using Eq. 8.

$$C_b^i = \begin{bmatrix} a^2 + b^2 - c^2 - d^2 & 2(bc + ad) & 2(bd - ac) \\ 2(bc - ad) & {}^2 - b^2 + c^2 - d^2 & 2(cd + ab) \\ 2(bd + ac) & 2(cd - ab) & a^2 - b^2 - c^2 + d^2 \end{bmatrix} \tag{8}$$

## 2. Specific Force Transformation

After the attitude has been updated, the next step in the INS mechanization is the transformation of the accelerometer measured specific force, or equivalently, incremental changes to the body-axis velocity $\Delta v_b$ into the inertial frame. This must be done because the accelerometers measures specific force along the body-axis; however, for the velocity update step the specific force must be in the inertial frame. The transformed $\Delta v_b$ can be found using Eq. 9 where $C_b^i$ is the body to inertial DCM of the INS updated quaternion from Eq. 8.

$$\Delta v^i = C_b^i \Delta v^b \tag{9}$$

## 3. Velocity Update

With the transformed specific force, the updated velocity is calculated using Eq. 10. Where the updated velocity is the summation of the previous velocity value $(k-1|k-1)$, the IMU measured change in velocity, $\Delta v^i$, and the acceleration due to gravity in the inertial frame, $\gamma^i$, integrated over the sampling interval $\tau$ .

$$v_{k|k-1}^i = v_{k-1|k-1}^i + \Delta v^i + \gamma^i \tau \tag{10}$$

## 4. Position Update

The final step in the INS mechanization is to calculate the updated position. The updated position estimate is a function of the previous position estimate and the average of the previous and updated velocity estimates integrated over the sampling interval.

$$r_{k|k-1}^i = r_{k-1|k-1}^i + (v_{k|k-1}^i + v_{k-1|k-1}^i)\frac{\tau}{2} \tag{11}$$

## 5. Attitude Transformation

In most aerospace applications, it is useful to represent the platform attitude with respect to a locally-level NED navigation frame. However, in the presented INS mechanization, a quaternion is used to represent the platform's attitude with respect to the Earth Centered Inertial (ECI) frame. To calculate the body-to-navigation Euler angles, the DCM must be transformed into the navigation frame. This is done using Eq. 12, where the Earth-Centered-Earth-Fixed (ECEF) to locally-level NED navigation ,$C_e^n$, and ECEF to inertial, $C_e^i$, transformations are defined in Eq. 13 and Eq. 14, respectively, which can be found in numerous texts.[15, 16]

$$C_b^n = C_e^n C_e^i C_b^i \tag{12}$$

$$C_e^n = \begin{bmatrix} \text{-sin(Lat)cos(Lon)} & \text{-sin(Lon)} & \text{-cos(Lat)cos(Lon)} \\ \text{-sin(Lat)sin(Lon)} & \text{cos(Lon)} & \text{-cos(Lat)sin(Lon)} \\ \text{cos(Lat)} & 0 & \text{-sin(Lat)} \end{bmatrix} \tag{13}$$

American Institute of Aeronautics and Astronautics

$$C_e^i = \begin{bmatrix} cos(\omega_{ie}(t-t_0)) & -sin(\omega_{ie}(t-t_0)) & 0 \\ sin(\omega_{ie}(t-t_0)) & cos(\omega_{ie}(t-t_0)) & 0 \\ 0 & 0 & 1 \end{bmatrix} \tag{14}$$

In Eq. 14, the Earth's rotation rate with respect to an ECI frame is represented by $\omega_{ie}$ and $t_o$ is the reference epoch at which the ECI and ECEF frame are co-incident (e.g. J2000 is a typical ECI realization). After transforming the body-to-inertial (i.e. ECI) DCM into the body-to-navigation (i.e. locally-level NED) DCM, the platform's traditional aircraft Euler angles are extracted using Eq. 15, Eq. 16, and Eq 17: where $C_b^n$ is the body to navigation DCM, and the number subscript corresponds to the row and column location within the DCM.[17]

$$\phi = \text{atan2}(C_{b\ 31}^n, C_{b\ 32}^n) \tag{15}$$

$$\theta = \text{acos}(C_{b\ 33}^n) \tag{16}$$

$$\psi = -\text{atan2}(C_{b\ 13}^n, C_{b\ 23}^n) \tag{17}$$

## C.   Error State Extended-Kalman Filter

Now that the PPP observation model and the INS mechanization have been explained, the data fusion architecture can be discussed. In this study, a tightly-coupled error-state extended Kalman filter is adopted from Groves.[16] A schematic of the tightly coupled PPP/INS integration architecture can be seen in Figure 1.
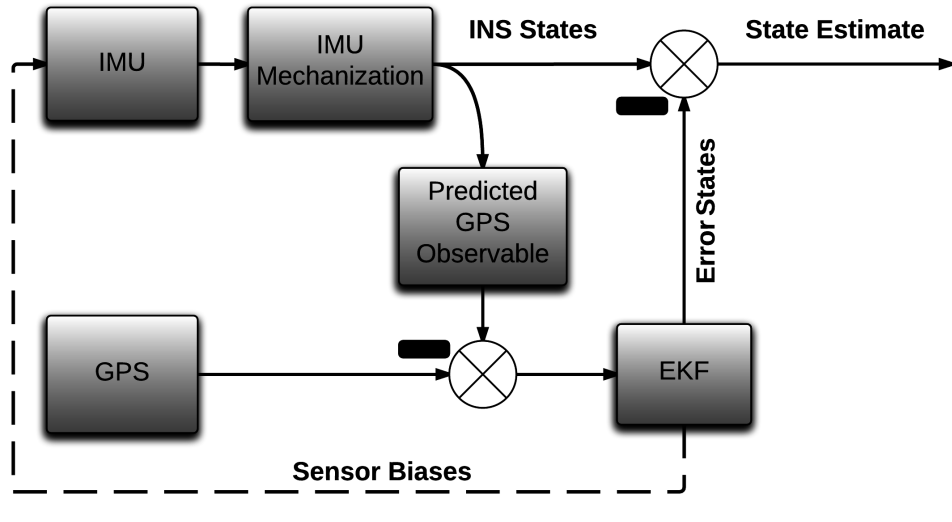


**Figure 1.  Tightly-Coupled GPS/INS**

Using the difference between the GPS observables and the INS predicted observables, the Kalman filter is used to estimate the INS solution errors with the state vector as shown in Eq. 18: where $\delta\Psi$ is the estimated attitude error, $\delta v$ is the estimated velocity error, $\delta r$ is the estimated position error, $b_a$ is the estimated accelerometer sensor biases, $b_g$ is the estimated gyroscope sensor biases, $\delta t_u$ is the estimated receiver clock bias, $T_w$ is the estimated residual tropospheric delay along the zenith direction, and $N$ is the estimated phase bias for each satellite in view.

American Institute of Aeronautics and Astronautics

$$\mathbf{x} = \begin{pmatrix} \delta \Psi \\ \delta v \\ \delta r \\ b_a \\ b_g \\ \delta t_u \\ T_w \\ N_1 \\ \vdots \\ N_j \end{pmatrix} \tag{18}$$

It can also be seen in Figure 1 that the estimated sensor biases are fed-back to correct the raw IMU measurements. Feedback is done at every time that a GPS update data is collected in a closed-loop manner. For the position and velocity estimated error states $\delta v$ and $\delta r$ are used to correct INS by subtracting them off of the INS estimated position and velocity. The attitude estimated error-state is applied to the INS attitude using a small-angle approximation as shown in Eq. 19

$$C_i^b = (I - \delta \Psi)\hat{C}_i^b \tag{19}$$

where $\hat{C}_i^b$ is the DCM populated with the INS estimated quaternion from Eq. 8.

To calculate INS error-state system matrix, $F$, the derivative of each error state model equation with respect to each error state must be taken. In this section, the time derivative of the attitude, velocity, and position are described. After defining the time derivatives of the error state equations, the total system matrix and the state transition matrix (STM) is defined.

The time derivative of the attitude error can be seen in Eq. 20: where $\hat{C}_b^i$ is the estimated body to inertial transition matrix, and $b_g$ is the estimated bias on the gyroscope.

$$\delta \dot{\Psi}^i = \hat{C}_b^i b_g \tag{20}$$

Because the velocity error is a function of the accelerometer bias, gyroscope bias, and the gravity model that is employed, it is slightly more complicated than the attitude error. The time derivative of the velocity error, $\delta \dot{V}^i$, can be seen in Eq. 21. In Eq. 21 $\hat{C}_b^i$ is the body to inertial frame transformation matrix, $\hat{f}^i$ is the IMU accelerometer measure specific force in the inertial frame $\delta v/\tau$, $\delta \Psi^i$ is the estimated attitude error, $g$ is the estimated gravity vector for the platforms position, $r_{es}^e$ is the geocentric radius at the platform position, $\hat{r}^i$ is the INS estimated position vector, $\delta r^i$ is the estimated position error, and $b_a$ is the estimated accelerometer sensor biases.

$$\delta \dot{V}^i = -(\hat{C}_b^i \hat{f}^i)\delta \Psi^i + \frac{2g}{r_{es}^e} \frac{\hat{r_{ib}^i}}{|\hat{r_{ib}^i}|^2} \hat{r}^{i\,T} \delta r^i + \hat{C}_b^i b_a \tag{21}$$

With INS mechanized in an inertial frame, the time-derivative of position is simply velocity. This means that the time-derivative of the position error in the inertial frame is the velocity error.

$$\delta \dot{r}^i = \delta V^i \tag{22}$$

Using the time derivative of each error state equation, the system matrix is defined in Eq. 23.

$$F^i = \begin{bmatrix} 0_3 & 0_3 & 0_3 & 0_3 & \hat{C}_b^i \\ -(\hat{C}_b^i \hat{f}^i) & 0_3 & \frac{2g}{r_{es}^e} \frac{\hat{r}^i}{|\hat{r}^i|^2} \hat{r}^{i\,T} & \hat{C}_b^i & 0_3 \\ 0_3 & I_3 & 0_3 & 0_3 & 0_3 \\ 0_3 & 0_3 & 0_3 & 0_3 & 0_3 \\ 0_3 & 0_3 & 0_3 & 0_3 & 0_3 \end{bmatrix} \tag{23}$$

American Institute of Aeronautics and Astronautics

The discrete System Transformation Matrix (STM) is then calculated using the system matrix and Eq. 24: where $F^i$ is the system matrix, and $\tau$ is the discretization interval. For this study, a third-order approximation of the STM was used as shown by the expansion in Eq. 25, as provided by Groves.[16]

$$\Phi = e^{F^i \tau} \tag{24}$$

$$\Phi^i = \begin{bmatrix} I_3 & O_3 & O_3 & O_3 & \hat{C}_b^i \tau \\ (F_{21}^i \tau + \frac{1}{6} F_{23}^i F_{21}^i \tau^2) & (I_3 + \frac{1}{2} F_{23}^i \tau^2) & (F_{23}^i \tau + \frac{1}{6} {F_{23}^i}^2 \tau^3) & (\hat{C}_b^i \tau + \frac{1}{6} F_{23}^i \hat{C}_b^i \tau^3) & (\frac{1}{2} F_{21}^i \hat{C}_b^i \tau^2) \\ (\frac{1}{2} F_{21}^i \tau^2) & (I_3 \tau + \frac{1}{6} F_{23}^i \tau^3) & (I_3 + \frac{1}{2} F_{23}^i \tau^2) & (\frac{1}{2} \hat{C}_b^i \tau^2) & (\frac{1}{6} F_{21}^i \hat{C}_b^i \tau^3) \\ 0_3 & 0_3 & 0_3 & I_3 & 0_3 \\ 0_3 & 0_3 & 0_3 & 0_3 & I_3 \end{bmatrix} \tag{25}$$

## III.   Simulation Environment

Using the models described in the previous section and a commercially available GPS constellation simulation toolbox, SatNav-3.04 Toolbox,[18] a simulation environment was developed to generate raw IMU and GPS data. The simulation environment architecture can be seen in Figure 2. This section will provide an overview of the simulation environment. First, we will discuss the inputs to the simulation, next we will provide an overview of the GPS data generation, and finally we will discuss the generation of the IMU data.
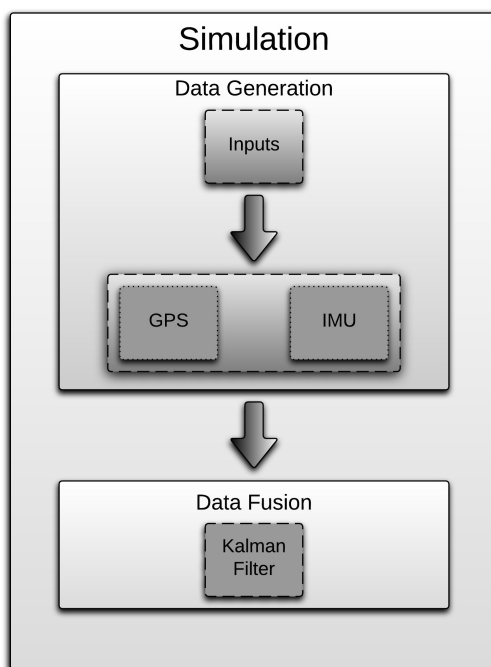


**Figure 2.  Flowchart Depicting the Simulation Environment**

### A.   Simulation Inputs

Before the generation of GPS and IMU data, several user-defined inputs are selected. One such input is the defined flight path. For this study, four flight paths of varying dynamics were designed to replicate typical data collection flights for NASA's UAVSAR airborne radar platform. As an example, two of the flight paths are shown in Figure 3 and Figure 4.

Other inputs that must be defined are the origin (e.g Lat., Lon., Height) of the flight and the time that the flight occurs. These parameters are randomized for every simulation run so that the generated data will have differing satellite geometry and atmospheric effects. In addition, the magnitude of the GPS error
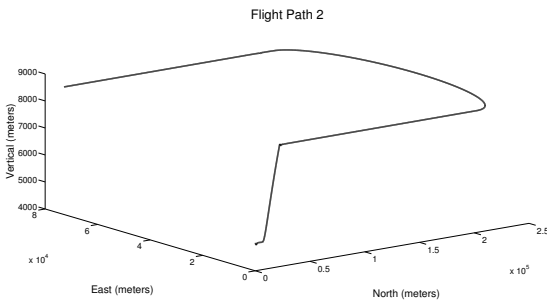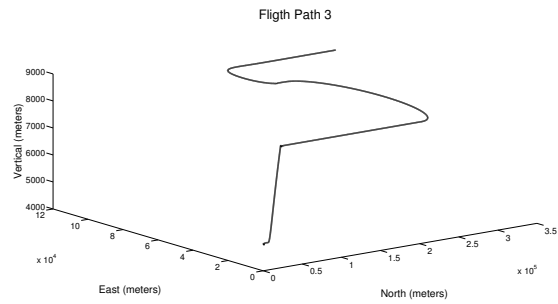
Figure 3.  Flight Path 2



Figure 4.  Flight Path 3

sources were selected before each simulation trial (e.g., multipath intensity, troposphere, and thermal noise). Finally, one of the four IMUs that were modeled for this study is selected for each run.

## B.   GPS Data Generation

Using the SatNav-3.04 Toolbox, dual-frequency pseudorange and carrier-phase observables are generated at 10 Hz over the specified flight path. For this study, modifications were made that are pertinent to common aircraft positioning error-sources. For example, the GPS simulator was modified to include attitude dependent satellite visibility masking and carrier-phase breaks. Figures 5 and 6 are included to depict the attitude dependent satellite masking. That is, when a satellite is obscured or nearly obscured due to a change in platform attitude, it is masked from view and the the potential of a carrier-phase breaks is increased. Figure 7 and Figure 8 are included to depict an example of carrier-phase breaks being added into the GPS data.
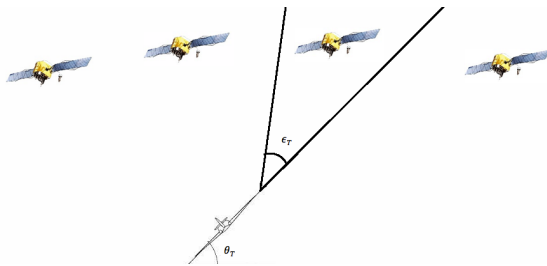


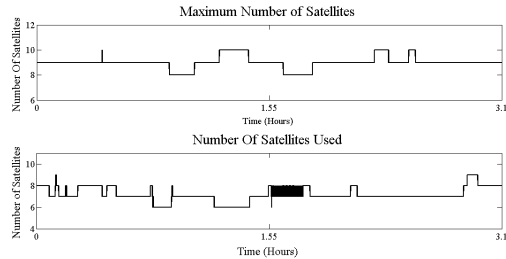Figure 5.  Attitude Dependent Satellite Masking



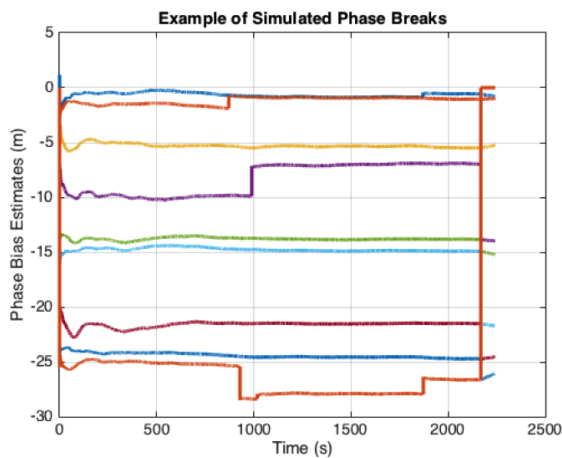Figure 6.  Number of Satellites in View for Flight
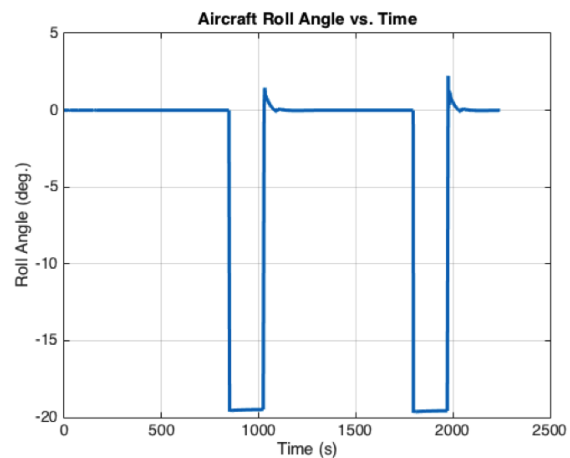


Figure 7.  Phase Breaks for an Example Flight



Figure 8.  Roll for an Example Flight

American Institute of Aeronautics and Astronautics

This simulation also includes an orbit and clock error model. The modeled errors were determined by differing JPL's International GNSS Service (IGS) submission with European Center for Orbit Determination (CODE) submission. The error between the satellite ephemeris products are resolved in the radial, in-track, and cross-track (RIC) components. After transforming the error into RIC components, it is fit using a multi-sinusodial model. This process was completed for each satellite. The modeled satellite clock bias can be seen in Fig. 9.
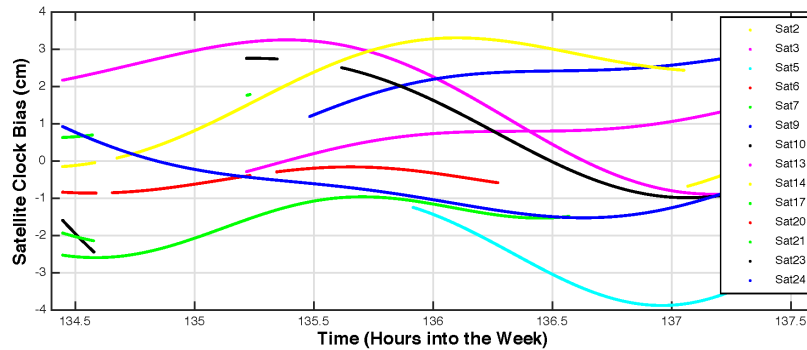


**Figure 9. Error Between Broadcast Products of IGS and CODE Products**

## C.    IMU Data Generation

To generate IMU data, a commercially available, tactical grade IMU was selected to model. The IMU was modeled with a turn-on bias, a random walk component, and white noise. The modeled IMU was scaled, with respect to Table 1, to simulated four IMUs of varying quality. The allan deviation of the four accelerometers and four gyroscopes along the x-axis for twelve hour of data can be seen in Figure 10.
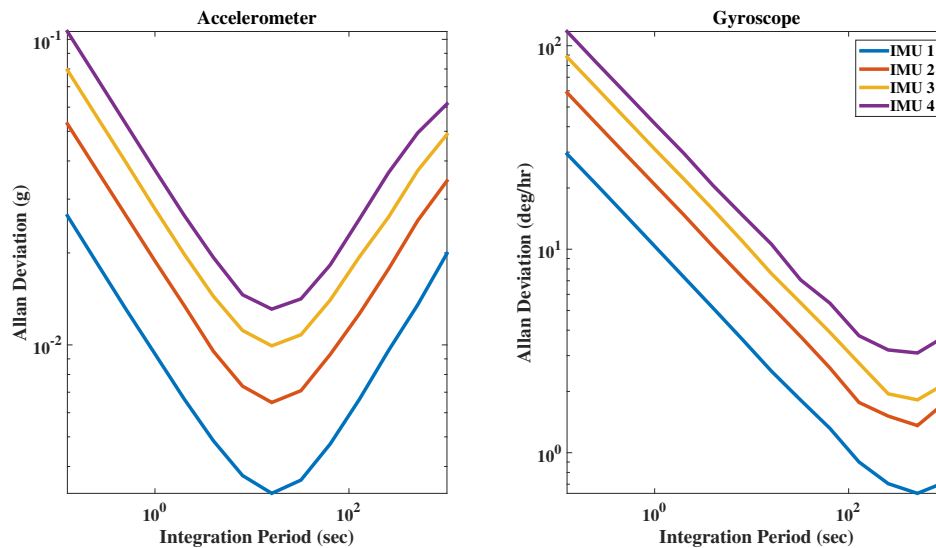


**Figure 10.    Allan Deviation for Accelerometer and Gyroscope**

## D.    Monte Carlo Study Design

To generate the results shown in the next section, a Monte Carlo style design was implemented. Each simulation trail was initialized at random across the distributions specified in Table 1. One hundred sets of data were generated. GPS and IMU data were generated for every flight at ten and two hundred hertz,

American Institute of Aeronautics and Astronautics

respectively. The one hundred data sets were run through a PPP only filter and a tightly-coupled PPP/INS filter to characterize the performance increase by including INS.

**Table 1. Simulation Parameters**

| Error-Sources | Model Parameters | Notes |
|---|---|---|
| **Accelerometer** | In-run Bias $\sigma = 1mg$ , $VRW = 0.2\frac{m/s}{\sqrt{hr}}$ | Scaled Honeywell HG1700AG72 SF $= (1, \frac{1}{50}, \frac{1}{200}, \frac{1}{400})$ |
| **Gyroscope** | In-run Bias $\sigma = 9.6e^{-6}\frac{rad}{sec}$ , $ARW = 0.2\frac{deg}{\sqrt{hr}}$ | Scaled Honeywell HG1700AG72 SF $= (1, \frac{1}{50}, \frac{1}{200}, \frac{1}{400})$ |
| **Thermal Noise** | $\sigma_\rho = 0.32m$ , $\sigma_\phi = 0.16\lambda$ | linear scale factor randomly selected between [0,1] |
| **Multipath** | 1.0 intensity: $\sigma = 0.4m, \tau = 15sec$ | linear scale factor randomly selected between [0,2] |
| **Tropospheric Delay** | Percent of error assumed handled by broadcast correction | Modified Hopfield with linear scale factor randomly selected between [0,1.5] |
| **Ionospheric Delay** | First order ionospheric effects mitigated with dual-frequency | linear scale factor randomly selected between [0.7,1] |
| **Receiver Clock Bias** | Initial Bias $\sigma = 30ns, \delta\tau_b = 100ns$ | Tuneable |
| **Phase Ambiguity** | Random initialization and phase breaks correlated with UAV attitude | likelihood varied from [0.008,0.02] |
| **Orbits** | Orbits $\sigma = 5cm$ | Description provided in section III.B |

American Institute of Aeronautics and Astronautics

# IV.   Results

## A.   Absolute Positioning Performance

To quantify the potential benefits of INS inclusion for UAV navigation in scenarios that typically degrade GPS performance, a sensitivity analysis of positioning performance was conducted under varying conditions. The metric used to quantify the error for the first nine figures in this section is Root Mean Square (RMS). The equation to calculate RMS can be seen in Eq. 26: where $n$ is the number of data points, $X$ is the actual value of the data, and $\hat{X}$ is the estimated value of the data.

$$X_{RMS} = \sqrt{\sum_{i=1}^{n} \frac{1}{n}(X^2(i) - \hat{X}^2(i))} \tag{26}$$

The median of the RMS positioning error for the one hundred flight can be seen in Fig. 11. From Fig. 11 it should be noted that the PPP/INS filter outperformed PPP only filter in east, north and vertical directions, with the most notable improvement being in the vertical direction. The statistics for the one hundred flights can be seen in Table 2, Table 3 and Table 4.
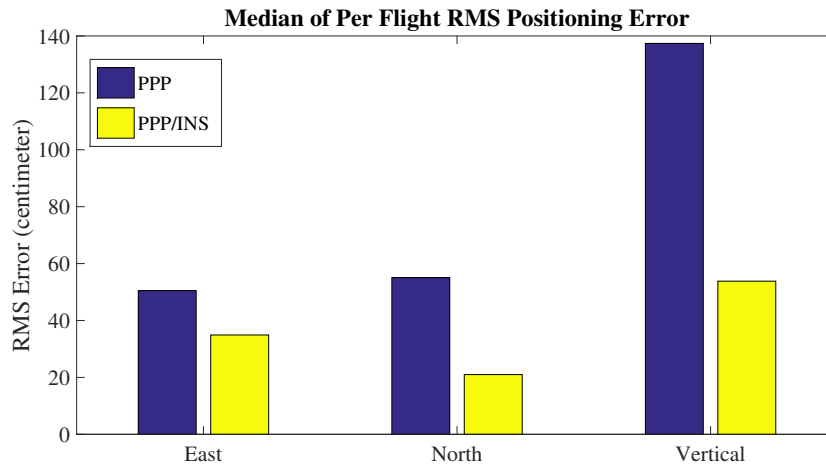


**Figure 11.   Median of Per Flight RMS Error**

|        | East (cm) | North (cm) | Vertical (cm) |
|--------|-----------|------------|---------------|
| Min    | 4.08      | 4.89       | 16.20         |
| Max    | 198.07    | 259.77     | 407.50        |
| Mean   | 62.85     | 65.25      | 146.52        |
| Median | 50.49     | 55.07      | 137.39        |
| Std    | 44.71     | 46.76      | 78.23         |

**Table 2.  PPP Only Statistics**

|        | East (cm) | North (cm) | Vertical (cm) |
|--------|-----------|------------|---------------|
| Min    | 5.65      | 2.94       | 17.15         |
| Max    | 137.36    | 121.80     | 310.95        |
| Mean   | 37.88     | 25.30      | 70.55         |
| Median | 34.90     | 20.99      | 53.82         |
| Std    | 24.23     | 19.38      | 55.81         |

**Table 3.  PPP/INS Statistics**

|        | East (cm) | North (cm) | Vertical (cm) |
|--------|-----------|------------|---------------|
| Min    | -55.42    | -64.12     | -206.92       |
| Max    | 158.02    | 221.40     | 343.94        |
| Mean   | 24.96     | 39.93      | 75.97         |
| Median | 16.94     | 31.76      | 69.62         |
| Std    | 32.65     | 38.75      | 85.31         |

**Table 4.  (PPP - PPP/INS) Statistics**

The next eight figures in this section depict the reduction in RMS error through the inclusion of INS. The reduction in error was calculated by taking the difference of the positioning output for the PPP only filter and the PPP/INS filter. Figure 12 shows the median of the per flight RMS error reduction due to the inclusion of INS.

From Fig. 12 it can be seen that the error reduction in the East, 17 centimeters, and North, 32 centimeters, directions are similar. The error reduction is the vertical direction is the most notable at 70 centimeters.

Figure 13 depicts the RMS error reduction distribution in the east, north and vertical directions for the 100 trials. This was done by calculating the cumulative distribution function (CDF) of the RMS positioning
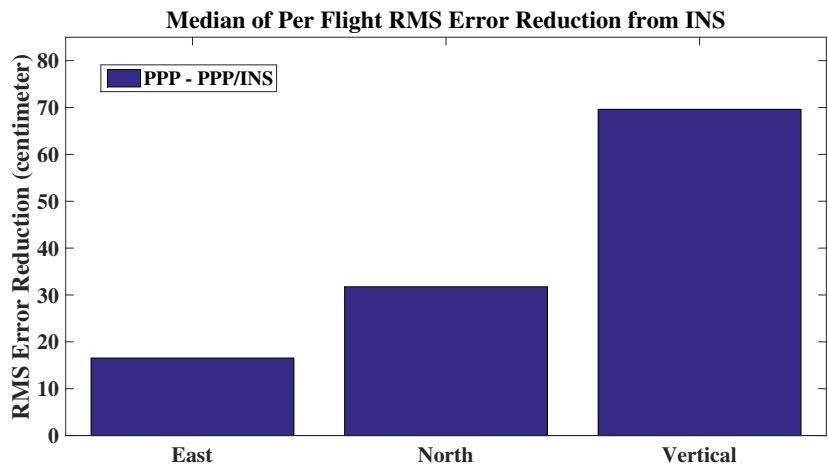
American Institute of Aeronautics and Astronautics

**Figure 12. Median of Per Flight RMS Error Reduction from INS**

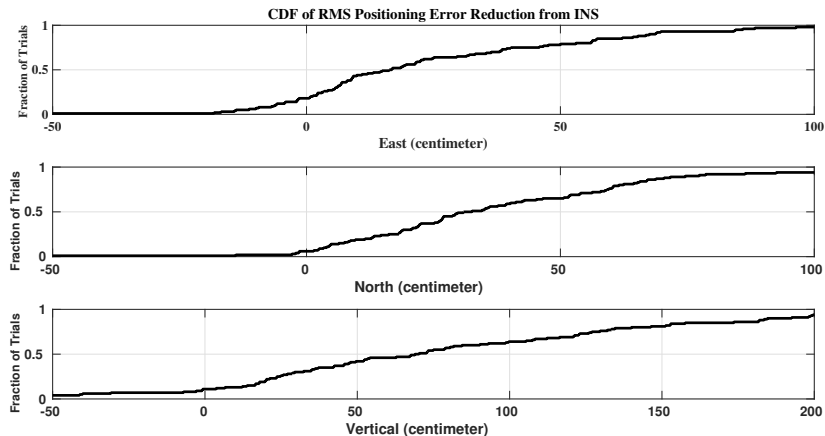error reduction for all of the simulated flight due to INS.



**Figure 13. CDF of RMS Positioning Error Reduction form INS**

From 13 it should be noted that the median error is as shown in Fig. 12; however, there are situations where the inclusion of INS can reduce the vertical positioning error by as much as 200 centimeters. However, there are times where the CDF is negative, meaning that the PPP-only filter outperformed the PPP/INS filter. For the cases in which PPP-only outperformance PPP/INS it is expected that that multiple satellite loss of lock or phase breaks may have occurred early in the filter run, before the phase biases, positioning, residual troposphere delay, and IMU sensor biases converged, leaving the PPP/INS solution to "hold on" to a poor solution for a longer period than the PPP-only filter; however these flights need further review.

Now that the median RMS error reduction has been discussed, it is of interest to discuss the reduction of the RMS error due to INS with respect to the input parameters (e.g., flight path, IMU selection and GPS error sources). Figure 14 shows the median RMS error reduction in the east, north and vertical directions with respect to the flight path selected. The four flight paths were designed to have increasing dynamics (i.e., flight path one is the most docile and flight path four has the highest dynamics). Figure 14 does not show a definitive trend in positioning improvement as path dynamics increase. The likely reason for this lack of trend is that the dynamics did not vary enough between paths.

Figure 15 shows the median RMS error reduction in the east, north and vertical directions with respect to the number of phase breaks during a flight. From Fig. 15 it should be noted that there is a clear correlation
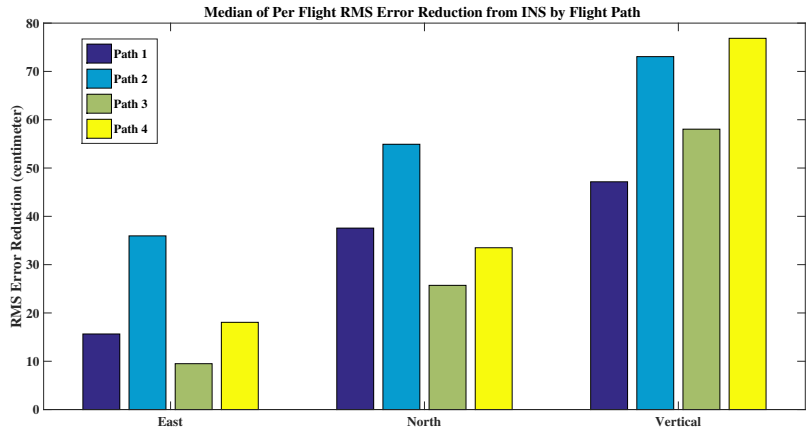
American Institute of Aeronautics and Astronautics

**Figure 14. Median of Per Flight RMS Error Reduction from INS by Flight Path**

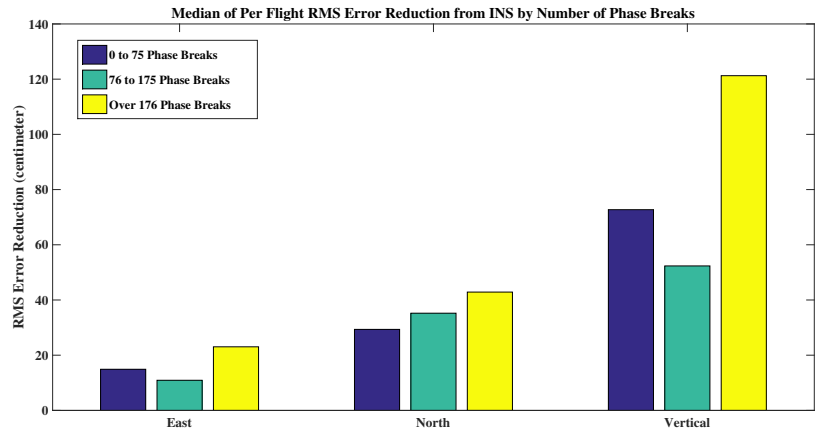between the number of phase breaks and the RMS positioning error reduction due to INS.



**Figure 15. Median of Per Flight RMS Error Reduction from INS by Number of Phase Breaks**

Figure 16 shows that median of the per flight RMS error reduction from INS by IMU type. As all of the IMUs for this study were modeled based upon error characteristics for commercially available tactical grade IMUs with similar error characteristics (e.g., all IMUs were scaled from IMU 1), there is not a definitive trend in positioning improvement.

Figure 17 depicts the RMS positioning error reduction due to INS with respect to the magnitude of the troposphere. Where the troposphere is modeled using the Modified Hopfield model and scaled at random, for each simulation trial, with respect to Table 1. From Fig. 17 a clear trend is shown, which is that the magnitude of the RMS error reduction is dependent upon the magnitude of the troposphere.

The dependence of the RMS positioning error reduction due to INS as a function of multipath can be seen in Figure 18. Multipath is modeled as a Gauss-Markov process with a standard deviation of 0.4 meters and a time constant of 15 seconds, as described in Table 1. This error source is linearly scaled for each simulation trial.

## B. Sensitivity to PPP Product Quality

Figure 19 depicts the benefit of including INS as the quality of the PPP products is reduced. That is, for this analysis, the GPS data was regenerated in the same manner as previously describe; however, the magnitude
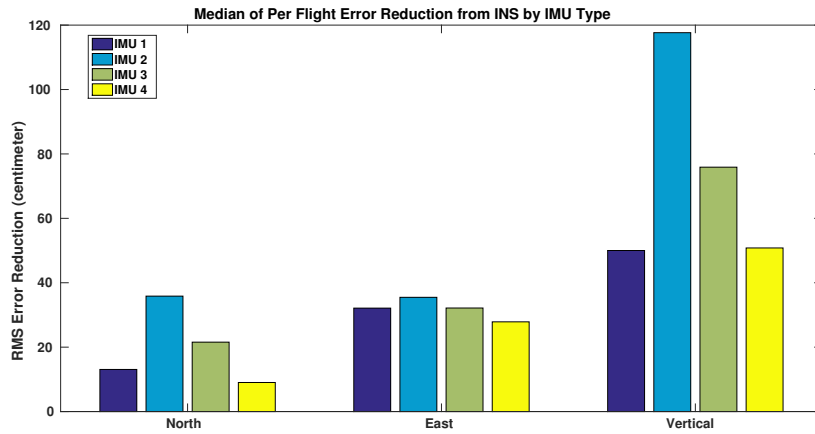
American Institute of Aeronautics and Astronautics

**Figure 16.  Median of Per Flight RMS Error Reduction from INS by IMU**
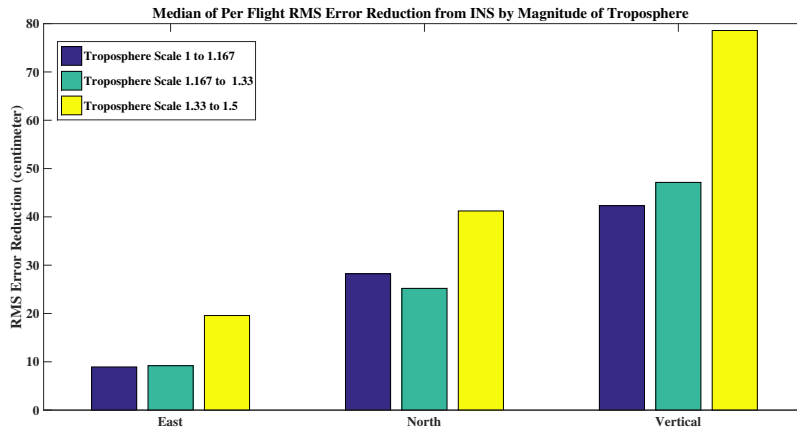


**Figure 17.  Median of Per Flight RMS Error Reduction from INS by Magnitude of Troposphere**
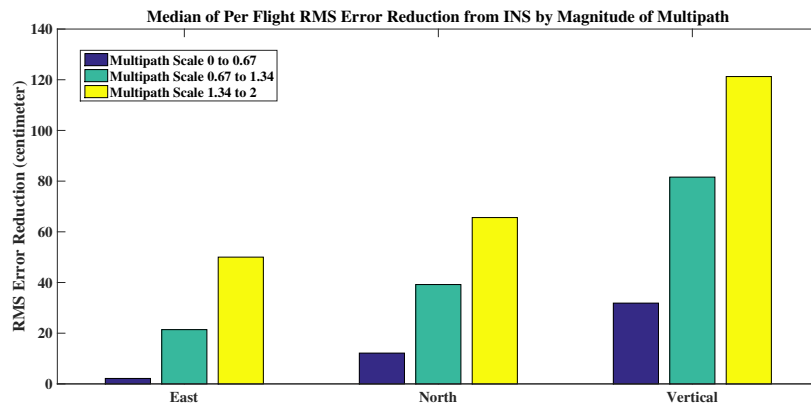


**Figure 18.  Median of Per Flight RMS Error Reduction from INS by Magnitude of Multipath**

American Institute of Aeronautics and Astronautics

of the satellite error was randomly selected from four magnitude (e.g., Product 1 = 0.5 cm, Product 2 = 10 cm, Product 3 = 20 cm, and Product 4 = 30 cm).
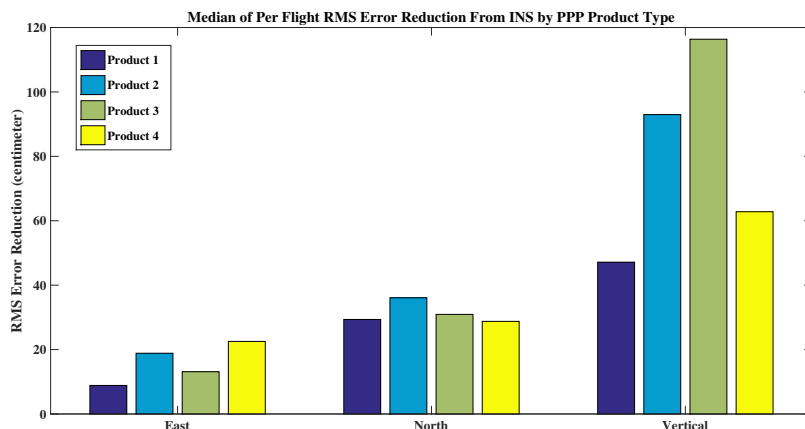


**Figure 19. Median of Per Flight RMS Error Reduction from INS by PPP Product**

## C. Attitude Estimation Performance

An implicit benefit of PPP/INS over single antenna PPP-only is that platform attitude is estimated in the filter. Figure 20 shows the typical attitude estimation performance of a single simulation trial.
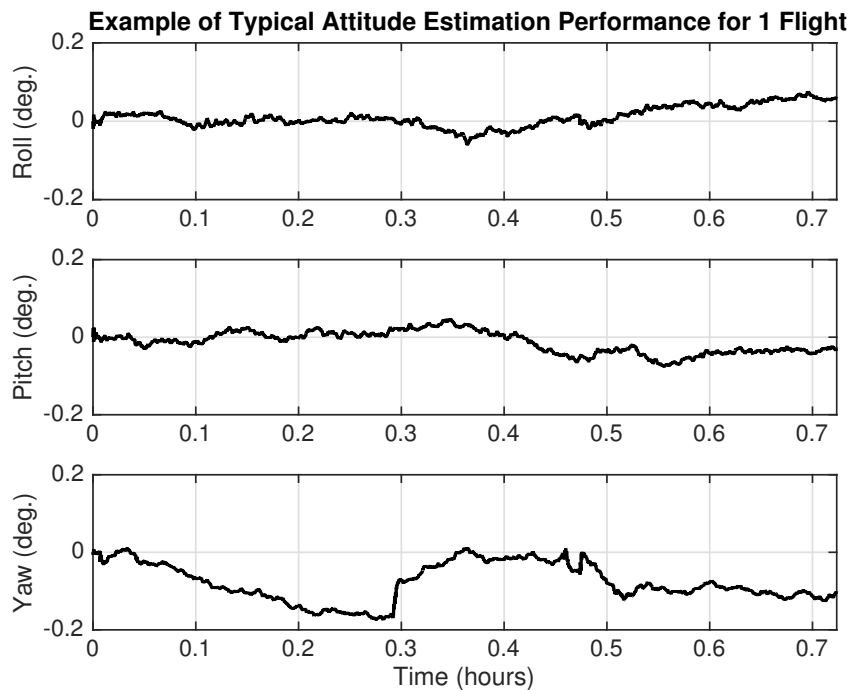


**Figure 20. Example Attitude Estimation Error over a Single Flight**

As shown in Fig. 20 roll, pitch and yaw are all estimated at sub-0.1 degree accuracy. A cumulative distribution of the attitude estimation performance of the 100 trials is shown in Fig. 21.

As illustrated in Fig. 21 the median attitude estimation error is a few hundredths of a degree for roll and pitch, and an order of magnitude worse for the yaw angle. Poor yaw estimation is expected for flight
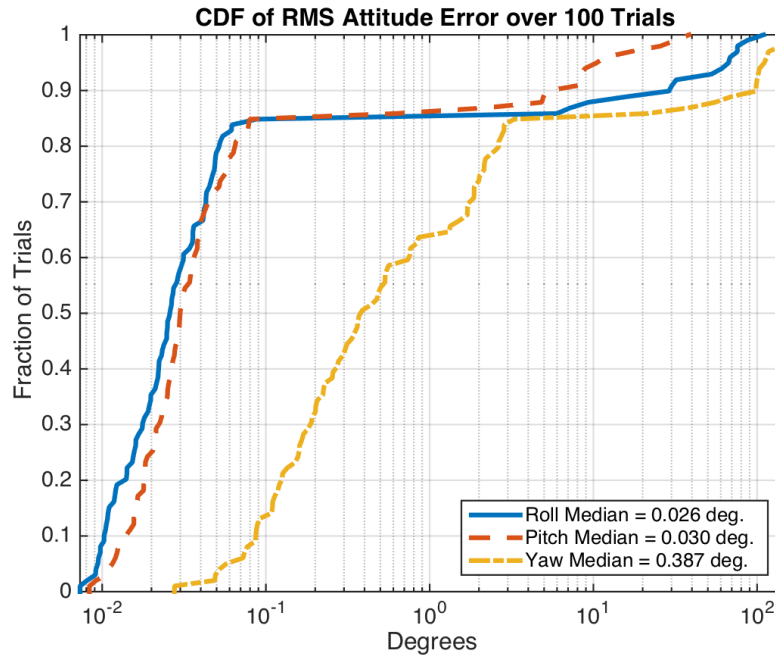
American Institute of Aeronautics and Astronautics

**Figure 21. Cumulative Attitude Estimation Performance over 100 Flights**

profiles that are predominately steady-level flight. Just as in positioning, there are a handful of PPP/INS flights that have poor attitude estimation performance.

## D. Solution Convergence

As mentioned in the literature review, PPP convergence is often cited as a downside to the PPP approach. Figure 22 was created by averaging the absolute phase bias estimate from the true simulated phases biases, epoch wise, for all 100 trials.
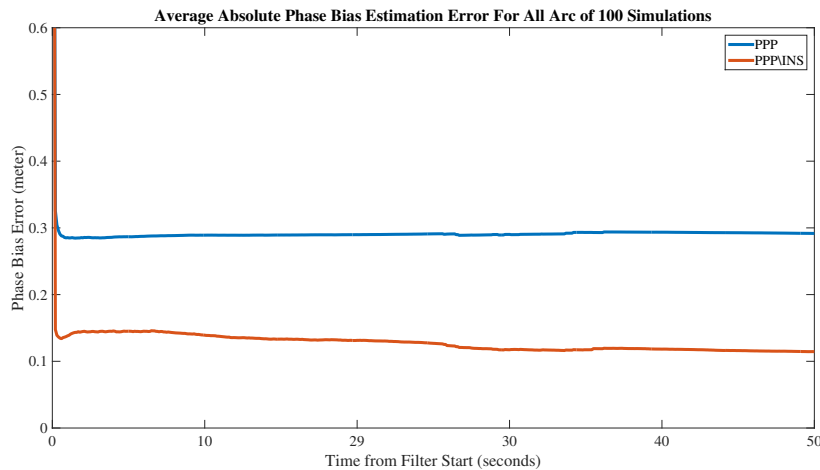


**Figure 22. Average Absolute Phase Bias Estimation Error**

As shown in Figures 22, the PPP/INS solution converges quicker than the PPP-only solution, which is important for reaching the performance similar to that of RTK.

American Institute of Aeronautics and Astronautics

### E. Smoothness of Positioning Solution

In general, the PPP/INS improvement is attributed to the smoother positioning performance. This claim can be substantiated by conducting a frequency analysis of the positioning error time-series. For example, Fig. 24 shows a periodogram of the amplitude of the position error in the vertical-axis for a typical flight trial. The periodogram can be evaluated up to 5Hz since the positioning residuals are available at 10Hz (i.e. the GPS update rate).
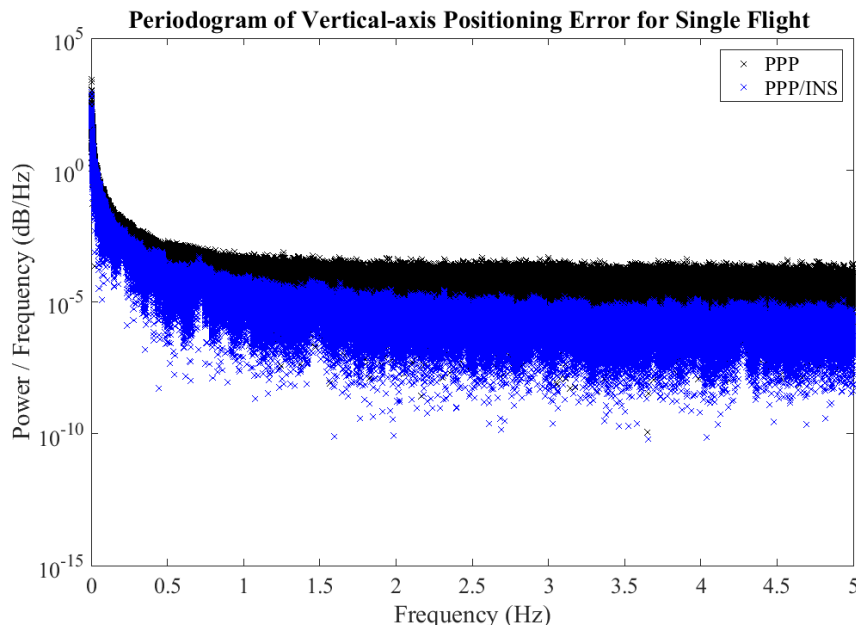


**Figure 23. Periodogram of Vertical Position Error for Single Flight**

As shown in Fig. 24, at the low frequencies the positioning performance is the same, and there is no noticeable difference in the absolute positioning performance, however, at the higher frequencies the PPP/INS error amplitude is reduced when compared to PPP. This analysis suggests smoother positioning from PPP/INS, which is critical for feedback control systems.

## V.   Conclusion

This article considered the performance sensitivity of PPP/INS and detailed the INS algorithm formulation that is currently being implemented in NASA JPL's RTG-X PPP software. The benefit of incorporating INS when confronted with scenarios that typically degrade GPS performance including poor satellite geometry and an increase level of phase breaks was characterized with the use of a Monte Carlo analysis. The inclusion of INS is shown to offer a smoother solution leading to better absolute positioning performance in an RMS and median sense over the 100 trials. PPP/INS also exhibited the ability to initially converge quicker, which is critical for PPP. In addition, the performance increase sensitivity for including tactical grade INS when confronted with poor PPP orbit product quality and increased path dynamics was demonstrated. In the future, this work will be further developed into an experimental evaluation of the presented approach using data collected by NASA's UAVSAR aircraft. Finally, this work will aid in the on-going effort to include high-grade INS processing within the Jet Propulsion Laboratory's RTG-X PPP software.

## Acknowledgments

American Institute of Aeronautics and Astronautics

# References

[1] Zumberge, J., Heflin, M., Jefferson, D., Watkins, M., and Webb, F., "Precise point positioning for the efficient and robust analysis of GPS data from large networks," *Journal of Geophysical Research: Solid Earth (1978–2012)*, Vol. 102, No. B3, 1997, pp. 5005–5017.

[2] Dixon, K., "StarFire: A global SBAS for sub-decimeter precise point positioning," *Proceedings of ION GNSS*, 2006, pp. 26–29.

[3] Muellerschoen, R. and Bar-Sever, Y., "Aviation applications of NASA's global differential GPS system," *Proceedings of the 2nd AIAA" Unmanned Unlimited" Conf. and Workshop & Exhibit, AIAA Paper*, Vol. 6618, 2003.

[4] "IGS Products," 2015.

[5] Rosen, P. A., Hensley, S., Wheeler, K., Sadowy, G., Miller, T., Shaffer, S., Muellerschoen, R., Jones, C., Zebker, H., and Madsen, S., "UAVSAR: a new NASA airborne SAR system for science and technology research," *Radar, 2006 IEEE Conference on*, IEEE, 2006, pp. 8–pp.

[6] Grewal, M. S., Weill, L. R., and Andrews, A. P., *Global positioning systems, inertial navigation, and integration*, John Wiley & Sons, 2007.

[7] Zhang, Y. and Gao, Y., "Performance Analysis of a Tightly Coupled Kalman Filter for the Integration of un-Differenced GPS and Inertial Data," *Proceedings of the 2005 National Technical Meeting of The Institute of Navigation*, 2001, pp. 270–275.

[8] Du, S. and Gao, Y., "Inertial aided cycle slip detection and identification for integrated PPP GPS and INS," *Sensors*, Vol. 12, No. 11, 2012, pp. 14344–14362.

[9] Du, S., *Integration of Precise Point Positioning and Low Cost MEMS IMU*, Master's thesis, University of Calgary, November 2010.

[10] Kjorsvik, N. S., Gjevestad, J. G. O., Broste, E., Gade, K., and Hagen, O.-K., "Tightly Coupled Precise Point Positioning and Inertial Navigation Systems," *International Society for Photgrammetry and Remote Sensing European Calibration and Orientation Workshop*, IPRS, 2010.

[11] Bar-Sever Y., B. W., Dorsey A., H. N., Lu, M. K., Miller M., R. L., Sibthorpe A., W. J., and Fernandez, M., G. J., "Real-Time and Post-Processed Orbit Determination and Positioning," 06 2015.

[12] Gross J., W. R., Sivaneri V., B.-S. Y., and Bertiger W., H. B., "Integration of Inertial Navigation into Real-Time GIPSY-X (RTGx)," *Institute of Navigation GNSS+*, Tampa, FL, 2015.

[13] Misra, P. and Enge, P., *Global Positioning System: Signals, Measurements and Performance Second Edition*, Lincoln, MA: Ganga-Jamuna Press, 2006.

[14] Kaplan, E. and Hegarty, C., *Understanding GPS: principles and applications*, Artech house, 2005.

[15] Jekeli, C., *Inertial navigation systems with geodetic applications*, Walter de Gruyter, 2001.

[16] Groves, P. D., *Principles of GNSS, inertial, and multisensor integrated navigation systems*, Artech House, 2013.

[17] Stevens, B. L. and Lewis, F. L., *Aircraft control and simulation*, John Wiley & Sons, 2003.

[18] GPSoft, "Satellite Navigation TOOLBOX 3.0 User's Guide," 2003.